Role of Oxygen Electrons in the Metal-Insulator Transition in the Magnetoresistive Oxide $La_{2-2x}Sr_{1+2x}Mn_2O_7$ Probed by Compton Scattering

B. Barbiellini,[1] A. Koizumi,[2] P. E. Mijnarends,[1,3] W. Al-Sawai,[1] Hsin Lin,[1] T. Nagao,[2] K. Hirota,[4] M. Itou,[5] Y. Sakurai,[5] and A. Bansil[1]

[1]*Physics Department, Northeastern University, Boston, Massachusetts 02115, USA*
[2]*Graduate School of Material Science, University of Hyogo, 3-2-1 Kouto, Kamigori-cho, Ako-gun, Hyogo 678-1297, Japan*
[3]*Department of Radiation, Radionuclides & Reactors, Faculty of Applied Sciences, Delft University of Technology, Delft, The Netherlands*
[4]*Department of Earth and Space Science, Graduate School of Science, Osaka University, 1-1 Machikaneyama, Toyonaka 560-0043, Osaka, Japan*
[5]*Japan Synchrotron Radiation Research Institute (JASRI), SPring-8, 1-1-1 Kouto, Sayo, Sayo, Hyogo 679-5198, Japan*

(Received 10 November 2008; published 20 May 2009)

We have studied the [100]-[110] anisotropy of the Compton profile in the bilayer manganite. Quantitative agreement is found between theory and experiment with respect to the anisotropy in the two metallic phases (i.e., the low temperature ferromagnetic and the colossal magnetoresistant phase under a magnetic field of 7 T). Robust signatures of the metal-insulator transition are identified in the momentum density for the paramagnetic phase above the Curie temperature. We interpret our results as providing direct evidence for the transition from the metalliclike to the admixed ionic-covalent bonding accompanying the magnetic transition. The number of electrons involved in this phase transition is estimated. Our study demonstrates the sensitivity of the Compton scattering technique for identifying the number and type of electrons involved in the metal-insulator transition.

DOI: 10.1103/PhysRevLett.102.206402 PACS numbers: 71.30.+h, 75.47.Gk, 75.47.Lx, 78.70.Ck

Recent developments in spin-based electronics or *spintronics* have revived the interest in manganites [1]. In particular, the bilayer manganites $La_{2-2x}Sr_{1+2x}Mn_2O_7$ (LSMO) show interesting colossal magnetoresistance (CMR) effects [2,3] in a complex phase diagram with charge and orbital ordering [4]. As seen in Fig. 1 of Ref. [3], the compounds in the doping range $x = 0.3$–0.4 show a metal-insulator transition (MIT) associated with the onset of long-range ferromagnetic (FM) order. The MIT occurs at a Curie temperature T_c of about 125 K (for $x = 0.35$) accompanied by colossal changes in the magnetoresistance [5,6]. Above T_c, the phase diagram displays an insulating paramagnetic (PM) phase. The Mn-3d electronic states, which are responsible for these properties, split into e_g and t_{2g} contributions in the crystal field of the MnO_6 octahedron. The FM phase below T_c and its metallic conductivity are usually explained on the basis of the double-exchange (DE) mechanism [7], where e_g electrons hop between Mn sites through hybridization with the oxygen $2p$ orbitals and align the localized t_{2g} spins by the exchange interaction. While the DE mechanism appears to capture the tendency towards ferromagnetism, it still remains unclear if oxygen orbitals should be explicitly included in the electronic degrees of freedom, or whether they can be integrated out as is often assumed in the standard models [8,9].

Recent magnetic Compton scattering (MCS) studies [10] of the manganite FM phase have shown how the occupation numbers of the e_g states vary with doping [11,12] as well as temperature [13,14]. In addition, they have provided evidence for the coexistence of localized and itinerant e_g magnetic electrons [15,16] in the FM phase. MCS has also been used to study other spintronics materials such as magnetite Fe_3O_4 and its mysterious Verwey transition [17].

In this Letter, we show that the anisotropy of high-resolution Compton profiles (CP) displays a striking difference between the insulating PM and metallic FM case. This is important because this difference originates in the MnO planes which are the seat of the CMR properties. Similar effects have been observed in the metallic $YBa_2Cu_3O_7$ and insulating $PrBa_2Cu_3O_7$ systems [18]. However, this is the first time that this effect has been observed on the same sample under the influence of external parameters such as temperature and magnetic field. We also provide a measure of the number of electrons involved in the CMR effect.

Compton scattering, or inelastic scattering with very high momentum and energy transfer, is a probe of the ground state one-electron properties of the system [10]. The measured one-dimensional quantity $J(p_z)$ is a projection of the three-dimensional electron momentum density $\rho(p_x, p_y, p_z)$ onto the z axis, which lies along the scattering vector:

$$J(p_z) = \iint \rho(p_x, p_y, p_z) dp_x dp_y. \quad (1)$$

The sample used was a single crystal of $La_{2-2x}Sr_{1+2x}Mn_2O_7$ with $x = 0.35$, which was melt-grown in flowing oxygen gas in a floating zone optical furnace [19]. According to the magnetic phase diagram

determined by neutron-diffraction measurements, the present sample shows a FM phase below 125 K [3]. High-resolution CP measurements were carried out with a Cauchois-type x-ray spectrometer installed on the BL08W beam line at SPring-8, Japan [19–22]. The energy of incident x rays was 115.6 keV and the scattering angle was 170°. The momentum resolution is estimated to be 0.15 a.u. CPs along the [100] and [110] axes were measured in three different conditions: the FM metallic state at low temperature (20 K), the CMR state in an external field of 7 T, and the PM insulating state at 131 K (above T_c).

The electronic structure, momentum density, and the CPs along principal symmetry directions used for analyzing the present measurements have been computed within an all-electron, fully charge and spin self-consistent semirelativistic Korringa-Kohn-Rostoker framework [23] for $LaSr_2Mn_2O_7$ in the $I4/mmm$ [24] crystal structure [12]. Our computed electronic structure (for $x = 0.5$) is in good accord with other studies [25,26]. The effects of doping x have been included within a rigid band model. All calculations agree on a nearly or wholly half-metallic FM band structure with the Fermi level crossing Mn d bands.

Since the LSMO electronic structure has a two-dimensional character, we shall focus on the calculated (001) 2D projection of the momentum density given by

$$\rho^{2D}(p_y, p_z) = \int \rho(p_x, p_y, p_z) dp_x. \tag{2}$$

Apart from Fermi surface (FS) effects, the calculated distribution $\rho^{2D}(p_y, p_z)$ contains some anisotropic components produced by the wave functions of the e_g and t_{2g} electrons. We extract the C_{4v} [27] anisotropy from $\rho^{2D}(p_y, p_z)$ by taking the difference

$$A^{2D}_{C_{4v}}(p_y, p_z) = \rho^{2D}(p_y, p_z) - \rho^{2D}\left(\frac{p_y + p_z}{\sqrt{2}}, \frac{p_y - p_z}{\sqrt{2}}\right). \tag{3}$$

The subtraction in Eq. (3) acts as a projector on the e_g and t_{2g} subspace with the advantage of eliminating the large isotropic contribution of the core and some irrelevant valence electrons. The anisotropy $A^{2D}_{C_{4v}}(p_y, p_z)$ shown in Fig. 1 displays a strong peak near (0.7, 0.7) a.u. which arises from wave functions of t_{2g} symmetry. On the other hand, there are peaks on the [100] axes at a distance of about 1.5 a.u. possessing e_g character and smaller peaks between 0.4 and 0.5 a.u. due to the oxygen p states at the FS. These oxygen p states hybridize with the e_g states of Mn. The amplitude of the t_{2g} and e_g peaks is about 9% of $\rho^{2D}(0, 0)$ while the amplitude of the p related peaks is less than 4%. As $A^{2D}_{C_{4v}}(p_y, p_z)$ integrates to zero, it assumes positive and negative values.

Interestingly, Fig. 1 displays the same sharp FS features, which appear in the calculated 2D projection of the spin momentum density onto the (001) plane [14]. In the present case, because of the definition of $A^{2D}_{C_{4v}}(p_y, p_z)$, we also have FS signatures rotated by 45° with respect to the original FS: These features come from the subtraction of the rotated two-dimensional distribution in Eq. (3). The large nested portions of the FS seen in Fig. 1 give maxima in the generalized charge susceptibility [28] and explain the interplay of the conduction electrons and lattice vibrations which contribute to the MIT [29]. However, our aim here is not to investigate these FS properties in detail but rather to show how Compton spectroscopy may be used to study bonding effects across the MIT in the bilayer manganites. In order to analyze bonding effects we now discuss the CP anisotropy [30], i.e., the difference between CPs measured in two crystallographic directions. In the present case, we consider

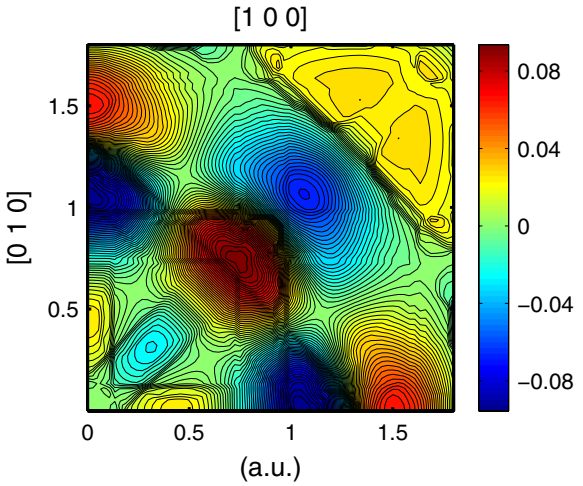

FIG. 1 (color online). Anisotropy $A^{2D}_{C_{4v}}(p_y, p_z)$ of the 2D projection of the theoretical electron momentum density onto the (001) plane, normalized to the amplitude $\rho^{2D}(0, 0)$.

$$A^{1D}(p_z) = J_{100}(p_z) - J_{110}(p_z). \tag{4}$$

Recalling from Eq. (1) that the CP involves a double integral, or equivalently, a 1D projection of the momentum density, the shape of $A^{1D}(p_z)$ can be computed from the 1D projection of the previous two-dimensional anisotropy $A^{2D}_{C_{4v}}(p_y, p_z)$ as

$$A^{1D}(p_z) = \int A^{2D}_{C_{4v}}(p_y, p_z) dp_y. \tag{5}$$

In Fig. 2, the profile $A^{1D}(p_z)$ shows the signatures of both the t_{2g} peak (at about 0.7 a.u.) and the e_g peak (at about 1.6 a.u.) discussed earlier and visible in Fig. 1. Figure 2 shows that at low momenta the anisotropy of the magnetic Compton profile $A^{1D}_{mag}(p_z)$ [12] (mostly of Mn-d character) is markedly different from $A^{1D}(p_z)$. Clearly, the nonmagnetic contribution due to the oxygen atoms is expected to give a more important impact at low momenta.

Next, we compare the calculated CP anisotropy with our measurements. In Fig. 3 all the *metallic* $A^{1D}(p_z)$ look

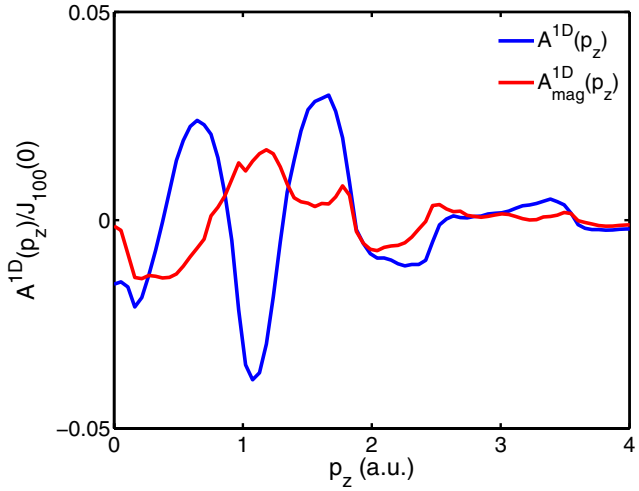

FIG. 2 (color online). Theoretical anisotropies $A^{1D}(p_z)$ and $A^{1D}_{mag}(p_z)$ [12] (without resolution broadening).

remarkably alike, showing that the overall description of the electronic structure is satisfactory. In particular, the amplitude of $A^{1D}(p_z)$ in the resolution-broadened theory is the same as that in the experiment, while in the case of the cuprates the theoretical $A^{1D}(p_z)$ had to be scaled down by a factor of 1.4 to obtain agreement with experiment [18]. The experimental curve for the *insulator* (paramagnetic phase), however, presents important changes in the low-momentum region indicating that the electrons with p oxygen character at the FS structure near $(0.5, 0)$ a.u. in Fig. 1 are significantly affected by the MIT. Moreover, the anisotropy for the insulator has a more pronounced positive excursion for $p > 4$ a.u.. This feature at high momenta is rather small in amplitude, but it causes the integrated anisotropy to be zero. These changes in $A^{1D}(p_z)$ can be explained in terms of a transition from metallic to admixed ionic-covalent Mn-O bonding [31]. According to the double-exchange mechanism [7], if the oxygen ion separates ferromagnetically coupled Mn^{3+} and Mn^{4+} in a lattice of disordered Mn ions, the state Mn^{3+}-O-Mn^{4+} is degenerate with the state Mn^{4+}-O-Mn^{3+} so that the d electrons develop a long-range phase coherence by hopping between Mn sites [7]. Therefore, in the FM phase below T_c, the bonding is metallic while in the PM phase above T_c the bonding becomes admixed ionic-covalent. The latter is described by a short-range phase coherence.

The wave function localization effects across the MIT can also be monitored by studying the power density [18]

$$P_D(z) = \left| \int dp_z A^{1D}(p_z) \exp(ip_z z) \right|^2. \quad (6)$$

The power density of the anisotropy separates in real space the different length scales contributing to the oscillations in the anisotropy in momentum. Thus, the peaks in the power density $P_D(z)$ indicate characteristic distances over which wave functions are coherent in given crystallographic directions. Figure 4 shows that the experimental data for the metallic phases and the theory are in agreement and that the wave functions are of a delocalized nature. However, the experiment for the insulator shows a clear tendency to shift spectral weight towards short distances. Thus, the localization trend for the insulator wave functions becomes clear. To ease the comparisons we have normalized all the power spectra to a unit area in Fig. 4 since only the relative weights in the same spectrum are relevant to study the localization [18].

The number of electrons involved in this localization can be extracted from the area enclosed by the anisotropy

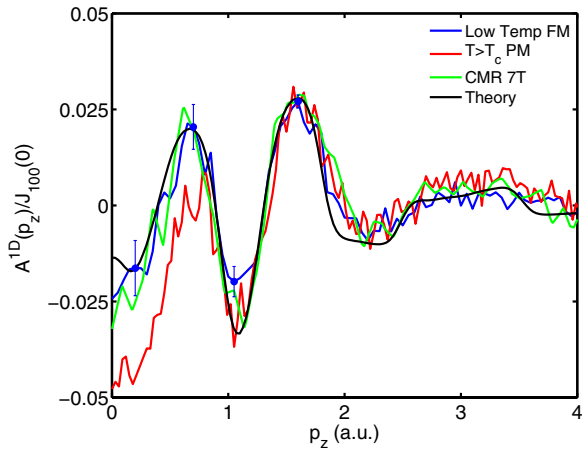

FIG. 3 (color online). Comparison of the theoretical and experimental $A^{1D}(p_z)$. In the legend, Low Temp FM is for the ferromagnetic phase at 20 K, $T > T_c$ PM is for the paramagnetic phase at 131 K, and CMR 7 T is for the colossal magnetoresistance phase in an external field of 7 T at 131 K. Theory is convoluted with the experimental resolution. Error bars shown for the FM phase are comparable for other experimental CP anisotropies.

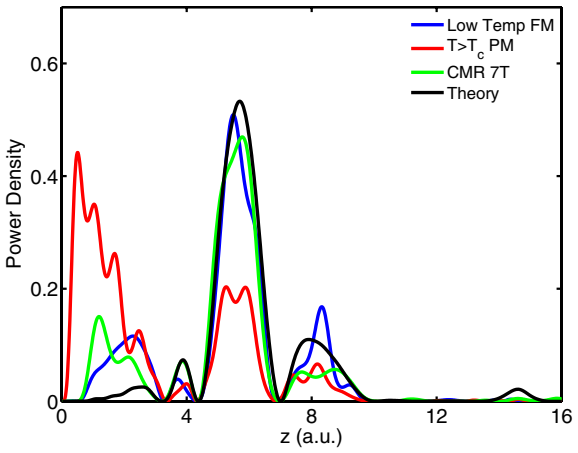

FIG. 4 (color online). Comparison of the theoretical and experimental $P_D(z)$. All the curves are normalized to a unit area. The notations in the legend are as in Fig. 3.

difference

$$\Delta A^{1D}(p_z) = A^{1D}_{PM}(p_z) - A^{1D}(p_z), \quad (7)$$

where $A^{1D}(p_z)$ is a metallic anisotropy (FM or CMR) and $A^{1D}_{PM}(p_z)$ is an insulating anisotropy. Therefore the quantity n_e given by

$$n_e = \frac{1}{2}\int dp_z |\Delta A^{1D}(p_z)| \quad (8)$$

measures the number of electrons whose wave functions change across the MIT. This is due to the shift of plane wave components from low to high momenta resulting in the wave function localization. We have normalized n_e to obtain the number of displaced electrons per Mn atom. The calculated values of n_e correspond to a displacement of 0.71 electron per Mn for the low-T FM-PM transition and of 0.67 electron per Mn for the CMR-PM transition These values are calculated from the anisotropies between 0 and 9.6 a.u. Their error is ± 0.08 based upon the statistical errors of the profiles. Thus, the present MIT gives particularly strong and robust signatures in momentum space.

In conclusion, our study shows that high-resolution Compton scattering spectra display striking features of the MIT and provide unique insights into the PM phase and the CMR effect in manganites. Ferromagnetism and metallic conductivity in the CMR phase are explained in terms of e_g long-range phase coherence produced by the DE mechanism. The momentum density anisotropy reveals that both the Mn and the oxygen orbitals play a key role in the MIT. By measuring the number of displaced electrons n_e across the MIT, the present method opens new opportunities for studying quantitatively the phase diagrams of complex materials.

We acknowledge discussions with Robert Markiewicz, Michael Kaplan, and Rolando Saniz. This work was supported by a Grant-In-Aid for Science and Culture, Japan, and by Contract No. DE-FG02-07ER46352 from the Division of Materials Science and Engineering, Office of Science, U.S. Department of Energy. It benefited from the allocation of supercomputer time at NERSC, the Northeastern University's Advanced Scientific Computation Center (ASCC), and the Stichting Nationale Computerfaciliteiten (National Computing Facilities Foundation, NCF). The Compton scattering experiments were performed with the approval of the Japan Synchrotron Radiation Research Institute (JASRI) (Proposals No. 2002B2008, No. 2003A3008, No. 2003B4008, and No. 2004A5008-LD3-np).

[1] M. I. Katsnelson *et al.*, Rev. Mod. Phys. **80**, 315 (2008).
[2] Y. Moritomo, A. Asamitsu, H. Kuwahara, and Y. Tokura, Nature (London) **380**, 141 (1996).
[3] M. Kubota *et al.*, J. Phys. Soc. Jpn. **69**, 1606 (2000).
[4] S. B. Wilkins *et al.*, J. Phys. Condens. Matter **18**, L323 (2006).
[5] T. Kimura *et al.*, Phys. Rev. Lett. **81**, 5920 (1998).
[6] D. N. Argyriou *et al.*, Phys. Rev. B **59**, 8695 (1999).
[7] C. Zener, Phys. Rev. **82**, 403 (1951).
[8] M. Coey, Nature (London) **430**, 155 (2004).
[9] E. Dagotto, New J. Phys. **7**, 67 (2005).
[10] M. Cooper *et al.*, *X-Ray Compton Scattering* (Oxford University, Oxford, 2004).
[11] A. Koizumi *et al.*, Phys. Rev. Lett. **86**, 5589 (2001).
[12] P. E. Mijnarends *et al.*, Phys. Rev. B **75**, 014428 (2007).
[13] A. Koizumi *et al.*, Phys. Rev. B **69**, 060401(R) (2004).
[14] Y. Li *et al.*, Phys. Rev. Lett. **93**, 207206 (2004).
[15] A. Koizumi *et al.*, Phys. Rev. B **74**, 012408 (2006).
[16] B. Barbiellini *et al.*, J. Phys. Chem. Solids **66**, 2197 (2005).
[17] Y. Li *et al.*, J. Phys. Chem. Solids **68**, 1556 (2007).
[18] A. Shukla *et al.*, Phys. Rev. B **59**, 12 127 (1999).
[19] K. Hirota *et al.*, J. Phys. Soc. Jpn. **67**, 3380 (1998).
[20] N. Hiraoka *et al.*, J. Synchrotron Radiat. **8**, 26 (2001).
[21] M. Itou and Y. Sakurai, AIP Conf. Proc. **705**, 901 (2004).
[22] Y. Sakurai and M. Itou, J. Phys. Chem. Solids **65**, 2061 (2004).
[23] A. Bansil, S. Kaprzyk, P. E. Mijnarends, and J. Toboła, Phys. Rev. B **60**, 13 396 (1999), and references therein.
[24] T. Hahn, *International Tables for Crystallography* (Reidel, Dordrecht, 1983).
[25] P. K. de Boer and R. A. de Groot, Phys. Rev. B **60**, 10 758 (1999).
[26] X. Y. Huang *et al.*, Phys. Rev. B **62**, 13 318 (2000).
[27] C_{4v} is the Schoenflies notation for a group containing a σ_v reflection in addition to C_4, a single fourfold axis symmetry; see, e.g., M. Tinkham, *Group Theory and Quantum Mechanics* (McGraw-Hill, New York, 1964).
[28] R. Saniz *et al.*, Phys. Rev. Lett. **101**, 236402 (2008).
[29] P. Littlewood and S. Kos, Nature (London) **438**, 435 (2005).
[30] E. D. Isaacs *et al.*, Phys. Rev. Lett. **82**, 600 (1999).
[31] J. B. Goodenough, Phys. Rev. **100**, 564 (1955).